Supporting Information for

Viscosity-dependent swimming patterns assist *Aliivibrio fischeri* for symbiont partner finding

Xiang-Yu Zhuang, Chao-Kai Tseng, and Chien-Jung Lo

Chien-Jung Lo.
E-mail: cjlo@phy.ncu.edu.tw

This PDF file includes:

Supporting text
Figs. S1 to S6
Legends for Movies S1 to S2
SI References

Other supporting materials for this manuscript include the following:

Movies S1 to S2

Supporting Information Text

Reconstructing image reference libraries of phase-contrast imaging system with real bacterial cells. We employ a high-throughput three-dimensional (3D) bacterial tracking method as originally described by Taute et al. (1). This technique relies on phase-contrast 3D tracking, which is based on the generation of an induced asymmetric point spread function (PSF) for determining the z-axis position (see Fig.S1A).

The images captured using a standard phase-contrast microscope are influenced by the optical path and the properties of the optical objective. Two crucial parameters to consider are the refractive index of the specimen (denoted as n_2) and that of the surrounding medium (n_1). It is important to note that the phase shift (δ), defined as $\delta = 2\pi \cdot \Delta/\lambda$, is a result of the optical path difference (Δ), where $\Delta = (n_2 - n_1) \cdot t$. Here, t represents the thickness of the specimen, and λ denotes the wavelength of the light used. To enhance image contrast, the phase shift is converted into an amplitude difference.

In their work, Taute et al. established a depth reference library using 1 µm silica beads (PSi-1.0, Kisker Biotech, Germany) (1). It is worth noting, however, that there is a significant difference in refractive index between bacteria (n = 1.384) (2, 3) and silica beads (n = 1.445) (4), as well as polystyrene beads (n = 1.591). When using 589 nm illumination light and considering that the width of *A. fischeri* is 0.83 µm, the phase shifts (δ) for *A. fischeri*, 1 µm silica beads, and 1 µm polystyrene beads are 0.14π, 0.38π, and 0.87π, respectively. Notably, there are significant discrepancies between the depth reference libraries of 1 µm polystyrene beads and *A. fischeri* (see Fig.S1B). This underscores the necessity of establishing dedicated bacterial depth reference libraries for precise z-position determination.

Mg^{2+}-regulated flagella number. The number of polar flagella in *A. fischeri* can be regulated by [Mg^{2+}] (0-50 mM) without impacting the cell growth and morphology. We conducted measurements of flagellar filament numbers and the distribution of swimming speeds under various regulatory media (Fig.S2). The flagellar count exhibits a direct correlation with magnesium concentration. At lower magnesium levels, *A. fischeri* tends to exhibit minimal growth and mainly has just a single flagellar filament. In contrast, under marine conditions with a magnesium concentration of 50 mM, *A. fischeri* consistently develops at least one or two flagella. The distribution of swimming speeds reveals two distinct populations, which can be effectively described by fitting a bimodal Gaussian function to the speed probability density function (Fig.S2A). We observed that swimming speed reached saturation when the [Na^{2+}] exceeded 30 mM. Typically, *A. fischeri* displays robust motility resembling that observed in natural marine environments when [Mg^{2+}] surpasses 2 mM. Regardless of flagellar number and energy conditions, the faster swimming speed is approximately twice as rapid as the slower swimming speed (Fig.S2B).

A high temporal-spatial resolution strobe fluorescence microscopy. The flagellar rotation speed of *A. fischeri* surpasses 200 Hz, as determined through back-focal-plane interferometry. This implies that the flagellar motor completes one revolution in less than 5 milliseconds. Conventional video-rate fluorescence imaging is unsuitable for capturing flagellar filament configurations because prolonged excitation times lead to the accumulation of flagellar motion, resulting in blurred images ((Fig.S3, red section). Let's assume that ten observation points are needed to document a single rotation. In this case, the acquisition rate should ideally exceed 2000 frames per second (fps) to provide a more detailed view of flagellar configurations. However, cameras with such high frame rates and large fields of view can be expensive and may pose phototoxicity risks to the cells. On the other hand, scientific complementary metal-oxide-semiconductor (sCMOS) cameras can achieve high frame rates up to kilohertz by reducing the region of interest (ROI). Unfortunately, reducing the ROI size does not offer any advantage when it comes to observing flagellar motion, as bacteria can quickly swim out of the observation field. The underlying concept of strobe fluorescent microscopy is to minimize excitation time to freeze transient motion while maintaining the camera frame rate (Fig.S3, green section). Strobe fluorescence microscopy can be readily implemented in standard fluorescence microscopes equipped with high-power LED or laser illuminations. It serves as an effective method for real-time observation of bacterial swimming modes.

More transitions example. We present examples of mode transitions, including transitions from push mode to wrap mode (Fig.S4) and transitions from wrap mode to push mode (Fig.S5).

Active particle model and Accumulation curves. We provide a concise summary of the swimming dynamics of *A. fischeri*. In low-viscosity environments, *A. fischeri* predominantly exhibits a switch between push-pull motions. As the viscosity of the environment increases, the likelihood of *A. fischeri* entering wrap modes becomes more pronounced. For our analysis, we focus exclusively on high-viscosity conditions, in which *A. fischeri* primarily displays push-wrap modes. Notably, our investigations revealed that *A. fischeri* can undergo synchronized flagellar polymorphic transitions and flagellar motor switching during wrap mode. To verify the advantages of this novel motility pattern in highly viscous environments, we constructed a mathematical model and conducted Brownian dynamic simulations. The numerical simulation procedure can be summarized as follows:

1.) We consider two distinct swimming modes for *A. fischeri*: forward (push) and backward (wrap).

2.) The rotational states of flagellar motors adhere to the CCW-CW-CCW-CW sequential rule. The run time τ follows an exponential distribution (5):

$$f(\tau) = \frac{1}{\tau_0} \cdot e^{-\frac{\tau}{\tau_0}} \quad [1]$$

Here, τ_0 represents the mean run time, while τ_0^{CCW} and τ_0^{CW} denote the mean run times for CCW and CW rotations, respectively.

3.) In our simplified model, *A. fischeri* initiates from the forward push mode (CCW, LH) and transitions to the backward wrap mode (CW, RH). During this phase, it has the option to either transit to another wrap mode (CCW, LH) with a probability of P_{sync} or return to push mode (CCW, LH) with a probability of 1-P_{sync}.

4.) When A. fischeri undergoes reversal-like swim direction changes, such as push-to-wrap or wrap-to-push transitions, the turning angle follows an exponential distribution with a mean angle of 150 ° (6):

$$f_\psi(\psi) = \frac{6}{\pi} \cdot e^{-\frac{6(\psi-\pi)}{\pi}} \quad [2]$$

Transitions between wrap modes (CW, RH) and (CCW, LH) do not impact the swimming direction.

5.) The spatial distribution of the attractant source is modeled as a time-independent 2-dimensional Gaussian distribution:

$$C(r_a) = C_0 \cdot e^{-\frac{(r_a - r_0^{che})^2}{2\sigma^2}} \quad [3]$$

, where r_0^{che} and σ denote the attractant center and the standard deviation of the Gaussian distribution, respectively.

6.) When virtual cells sense attractant concentrations exceeding 0.1 μM (7), the average run time of CCW rotation (τ_0^{CCW}) is determined by a gain function (8):

$$(\tau_0^{CCW})_{che} = \tau_0^{CCW} \cdot \frac{A}{1 + Be^{-KC}} \quad [4]$$

Here, K represents the motor gain value, while A and B are parameters fitted to match our experimental data.

7.) If virtual cells sense an increase in attractant concentration, the CCW cycle follows the aforementioned rules. Otherwise, counterclockwise motion halts with a response time of 0.4 seconds (7). Furthermore, the saturating concentration of chemotactic receptors is limited to 100 μM (9).

8.) The positions of the cells are updated in accordance with the rules described above.

Accumulation function. The process of accumulation can be further analyzed as the accumulation of random walkers within a defined area. We assume that the probability of locating bacteria follows a 2-dimensional time-dependent Gaussian diffusion equation:

$$n(r,t) = \frac{1}{4\pi Dt} \cdot e^{-\frac{(r - r_0^{cell})^2}{4Dt}} \quad [5]$$

Here, r represents the current position of bacteria, and r_0^{cell} denotes the initial position of the bacteria. We can then integrate this diffusion formula to obtain the accumulation probability within the attraction region $\Re$:

$$N(\Re, t) = \int n(r,t) \mathrm{d}t \mathrm{d}\Re \quad [6]$$

We refer to $N(\Re, t)$ as the time-dependent accumulation function, and the attraction region $\Re$ is defined as the region with the minimal attraction concentration:

$$0 < r < r_{min}^{response} = r_0^{che} + \sqrt{-2\sigma^2 \cdot \ln \frac{C_{min}^{response}}{C_0}} \quad [7]$$

Assuming the initial location of bacteria is far from the attractant source, we can rewrite the tail of the Gaussian function as a constant term. In this case, the accumulation probability can be calculated as:

$$N(\Re, t) = \left[\frac{1}{4\pi D} \cdot \ln \frac{4Dt}{r_0^2} - \frac{1}{4\pi D} \cdot \sum_{m=1}^{\infty} \frac{(-\frac{r_0^2}{4Dt})^m}{m \cdot m!} + (Const.) \right] \cdot \left[\pi (r_{response}^{min})^2 \right] \quad [8]$$

When t significantly exceeds t_0 (defined as $r_0^2/4D$), we can derive an approximate accumulation probability within the observation region as:

$$N(\Re, t) \approx \frac{(r_{response}^{min})^2}{4D} \cdot \ln \frac{4Dt}{r_0^2} \quad [9]$$

Furthermore, bacteria begin to accumulate when t is greater than or equal to t_0:

$$N(\Re, t) \propto \ln t \quad [10]$$

The accumulation function for cells under various parameters, including P_{sync}, L, versus time is shown in Figure (Fig.S6).

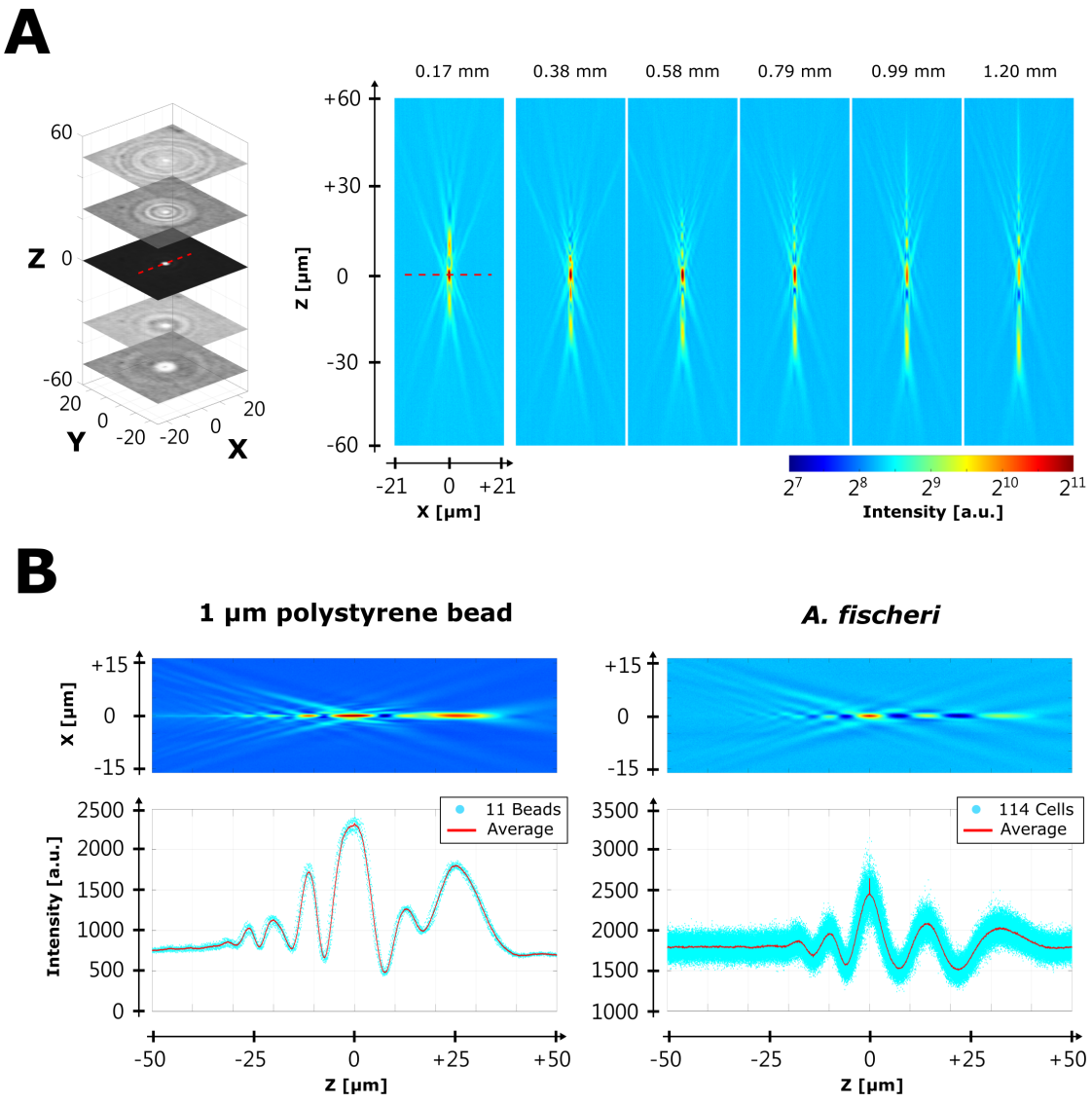

Fig. S1. Image Reference Libraries. (A) Left: A 3D image of the reference stacks for cells. Right: Comparison of image reference libraries obtained with various correction collar settings. (B) Comparison of image reference libraries created using 1 µm polystyrene beads and *A. fischeri* cells.

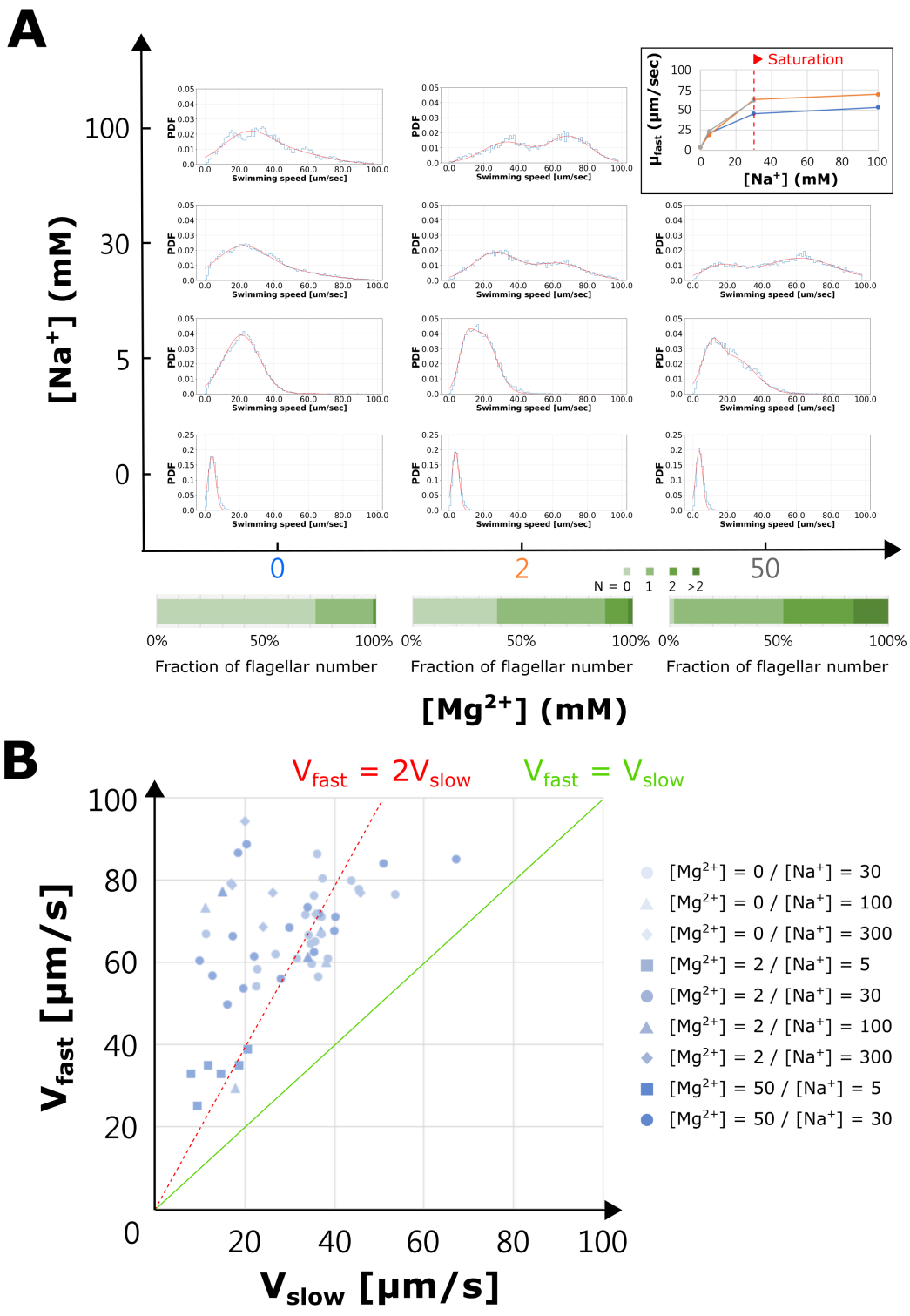

Fig. S2. Swimming Speed Analysis. (A) Histograms depicting swimming speeds under varying flagellar numbers and sodium concentrations. (B) A comparison of two swimming speeds under different sodium and magnesium concentrations. Concentration units are expressed in millimolars (mM).

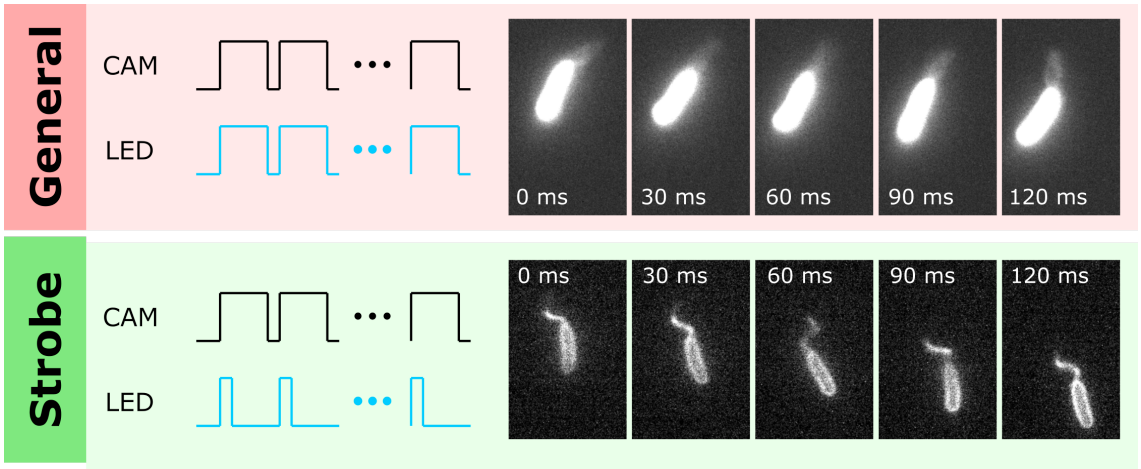

Fig. S3. Comparison of *A. fischeri* flagellar motion in fluorescence images. Fluorescence images capturing *A. fischeri*'s flagellar motion, using both standard (30 milliseconds) and strobe (150 microseconds) excitation techniques, captured at a frame rate of 33 frames per second (fps).

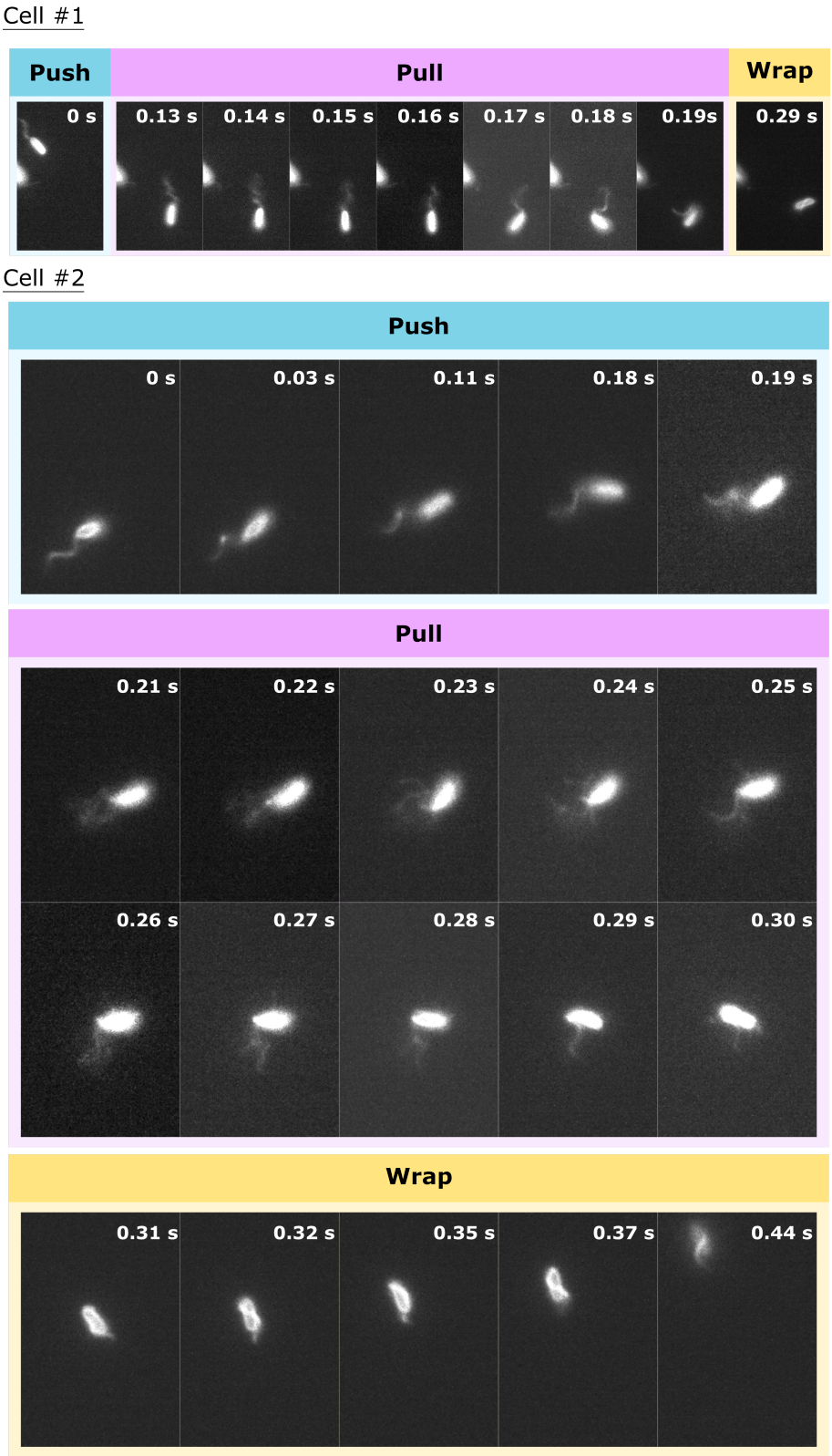

Fig. S4. Transitions to Wrap Mode. In Cell 1, the sequence illustrates transitions from push mode to pull mode and then to wrap mode, with all flagella forming a bundle. In Cell 2, the same transition sequence is observed; however, the flagella bundle disassembles during the pull mode and reassembles into a bundle during the wrap mode.

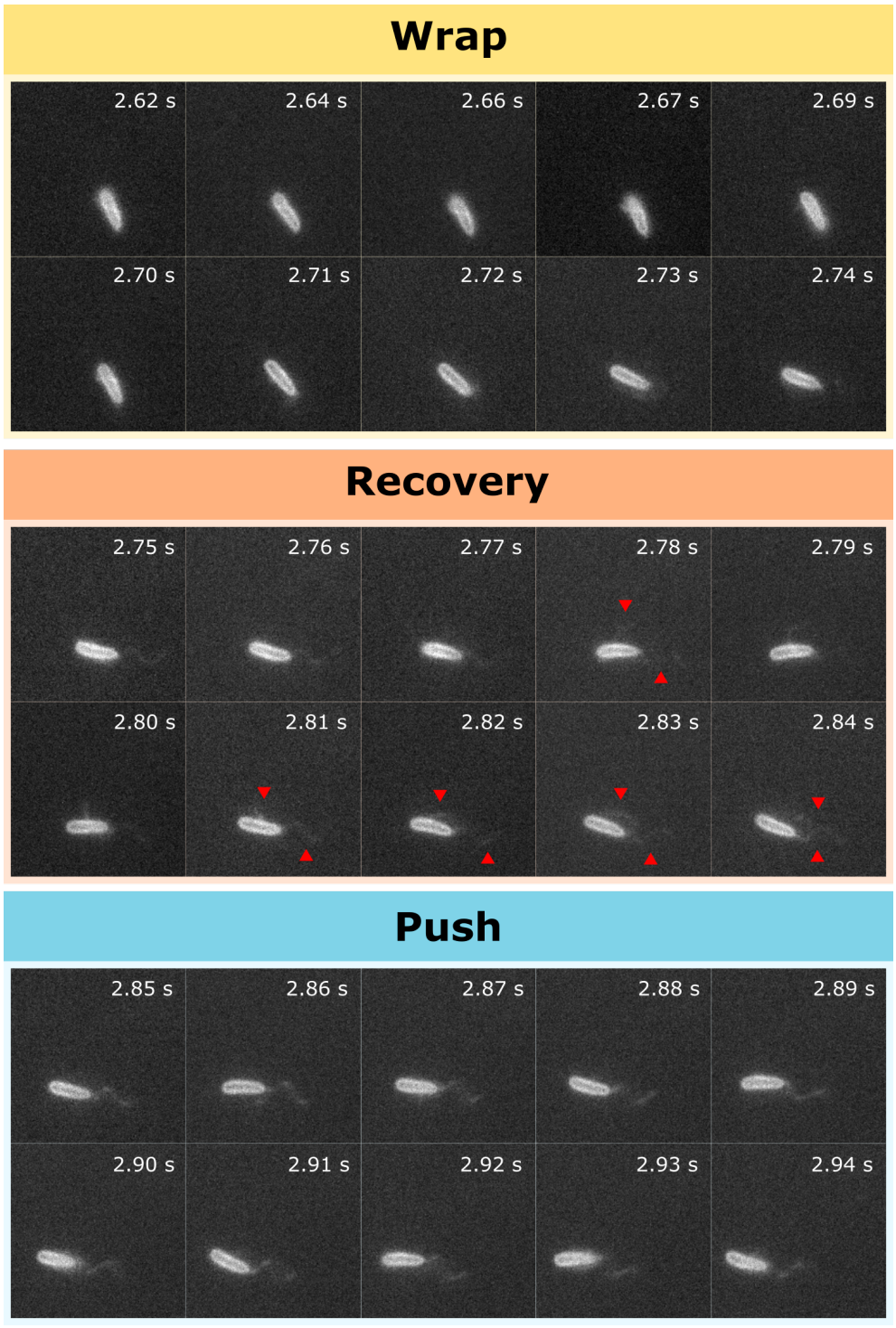

Fig. S5. Transition from Wrap to Push Mode. The cell exhibits a flagellar bundle during the wrap mode. At 2.78 seconds, the first flagellum departs from the bundle, followed by the second flagellum during the recovery process. Eventually, these flagella rejoin into a polar bundle, and the cell resumes the push mode.

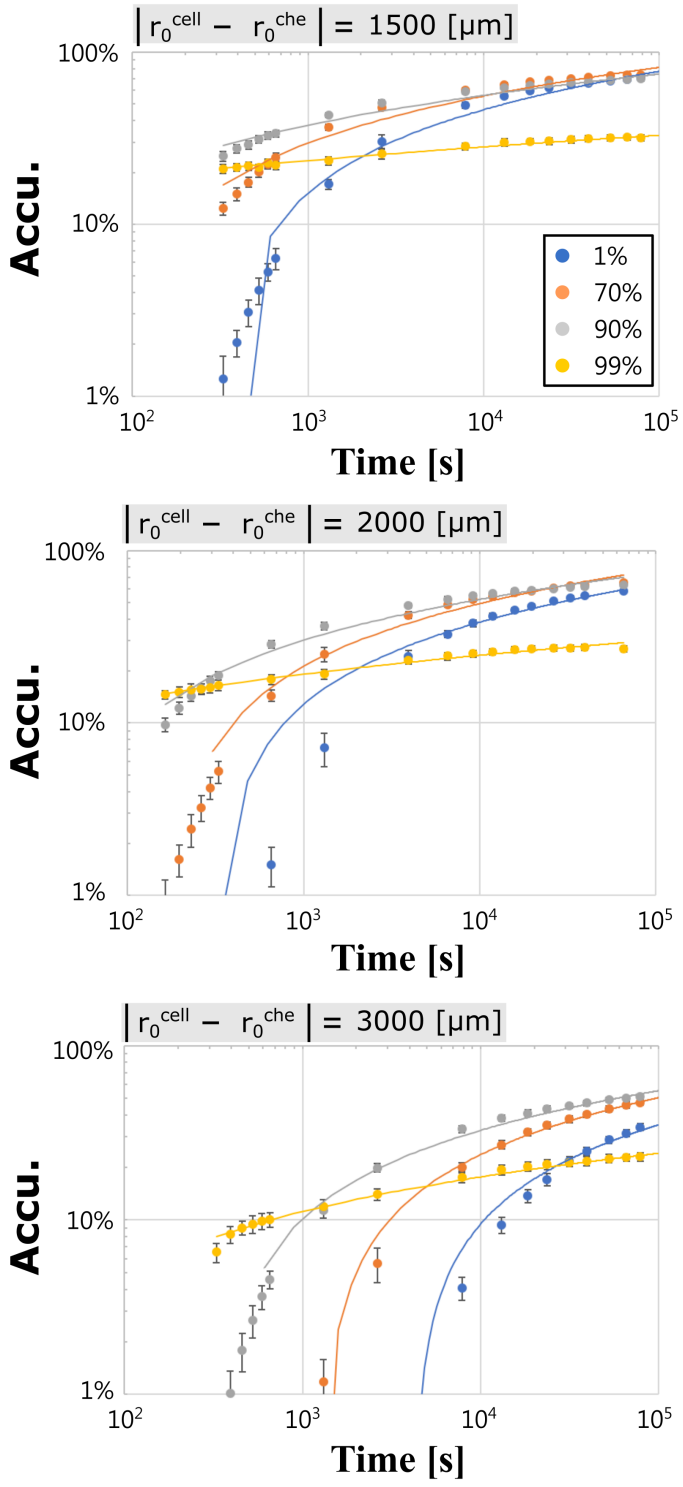

Fig. S6. Comparison of accumulation efficiency at a fixed Distance from the attractant source for Various synchronization probabilities. The solid line represents the fitted curve, while the discrete points represent simulated data points.

Movie S1. Strobe fluorescence images of real-time swimming configurations in *Aliivibrio fischeri* within a medium of viscosity 0.89 cP. The full HD images were captured with a field of view measuring 124.8 µm (width) by 70.2 µm (height) at a frame rate of 33.3 frames per second (fps) and an illumination time of 150 µs. Playback is shown at half-speed (1/2x).

Movie S2. Polymorphic transitions to extended wrap mode duration in *Aliivibrio fischeri*. Playback is shown at one-sixth speed (1/6x).

References

1. K Taute, S Gude, S Tans, T Shimizu, High-throughput 3d tracking of bacteria on a standard phase contrast microscope. *Nat. communications* **6**, 1–9 (2015).
2. AE Balaev, K Dvoretski, VA Doubrovski, Refractive index of escherichia coli cells in *Saratov Fall Meeting 2001: Optical Technologies in Biophysics and Medicine III*. (SPIE), Vol. 4707, pp. 253–260 (2002).
3. P Liu, et al., Real-time measurement of single bacterium's refractive index using optofluidic immersion refractometry. *Procedia Eng.* **87**, 356–359 (2014).
4. IH Malitson, Interspecimen comparison of the refractive index of fused silica. *Josa* **55**, 1205–1209 (1965).
5. Q Cai, Z Li, Q Ouyang, C Luo, VD Gordon, Singly flagellated pseudomonas aeruginosa chemotaxes efficiently by unbiased motor regulation. *MBio* **7**, e00013–16 (2016).
6. Z Alirezaeizanjani, R Großmann, V Pfeifer, M Hintsche, C Beta, Chemotaxis strategies of bacteria with multiple run modes. *Sci. advances* **6**, eaaz6153 (2020).
7. T Sagawa, et al., Single-cell e. coli response to an instantaneously applied chemotactic signal. *Biophys. journal* **107**, 730–739 (2014).
8. DR Brumley, et al., Bacteria push the limits of chemotactic precision to navigate dynamic chemical gradients. *Proc. Natl. Acad. Sci.* **116**, 10792–10797 (2019).
9. V Sourjik, HC Berg, Receptor sensitivity in bacterial chemotaxis. *Proc. Natl. Acad. Sci.* **99**, 123–127 (2002).